AGU PUBLICATIONS

Geochemistry, Geophysics, Geosystems

RESEARCH ARTICLE
10.1002/2013GC005151

Dynamic lithosphere within the Great Basin

Ryan C. Porter[1,2], Matthew J. Fouch[1], and Nicholas C. Schmerr[1,3]

[1]Department of Terrestrial Magnetism, Carnegie Institution of Washington, Washington, D. C., USA, [2]Now at School of Earth Science and Environmental Sustainability, Northern Arizona University, Flagstaff, Arizona, USA, [3]Department of Geology, University of Maryland, College Park, Maryland, USA

Key Points:
- The Great Basin structure is analyzed using multiple seismic imaging techniques
- Chemical and thermal lithosphere persist beneath western North America
- Downwellings have modified the Great Basin lithosphere

Correspondence to:
R. C. Porter,
Ryan.Porter@nau.edu

Citation:
Porter, R. C., M. J. Fouch, and N. C. Schmerr (2014), Dynamic lithosphere within the Great Basin, *Geochem. Geophys. Geosyst.*, *15*, 1128–1146, doi:10.1002/2013GC005151.

Received 15 NOV 2013
Accepted 1 MAR 2014
Accepted article online 5 MAR 2014
Published online 22 APR 2014

Abstract To place new constraints on the short-term, broad-scale lithospheric evolution of plate interiors, we utilize broadband seismic data from the Great Basin region of the Western United States to produce high-resolution images of the crust and upper mantle. Our results suggest that parts of the Great Basin lithosphere has been removed, likely via inflow of hot asthenosphere as subduction of the Farallon spreading center occurred and the region extended. In our proposed model, fragments of thermal lithosphere removed by this process were gravitationally unstable and subsequently sank into the underlying mantle, leaving behind less dense, stronger, chemically depleted lithosphere. This destabilization process promotes volcanism, deformation, and the reworking of continental lithosphere inboard from plate margins. Our results provide evidence for a new mechanism of lithospheric evolution that is likely common and significant in postsubduction tectonic settings.

1. Introduction

Earth's tectonic plates are continuously evolving through rifting, collision, and destruction via subduction. Over long time and orogen-wide scales, these processes are relatively well understood as plate geometries and interactions are traceable back on continental scales as far as ~2.1 Ga [e.g., *Zhao et al*., 2004]. Over these time and spatial scales, tectonic plates are considered as a single unit without significant lateral or radial complexity. Over shorter time periods and smaller geographic areas, the evolution of plate boundaries is often more enigmatic, as complete geologic records at these scales are often less well preserved. Furthermore, lithospheric heterogeneities must be considered when explaining tectonic processes at these smaller scales.

Taking this into account, we use receiver functions and surface wave tomography, calculated from both ambient noise and earthquake-generated surface waves, to explore the crustal and upper mantle structure of the central Great Basin. To place our observations in the context of western North American tectonics, we use the concept of heterogeneities in mantle-lithosphere chemistry to explain regional variations in lithospheric structure and dynamics based on geodetic and seismic observations, and argue that these control regional deformation, volcanism, and seismicity. Specifically, we suggest that two types of mantle lithosphere, thermal and chemical, existed within the region [e.g., *Yuan and Romanowicz*, 2010b]. Both types of lithosphere behave rheologically as part of semirigid tectonic plates and exhibit similar shear velocities [*Deschamps et al*., 2002]; however, they are distinguished by their chemistry, the manner in which they formed, their buoyancy, and their resistance to deformation. Chemical lithospheric mantle is depleted and forms during the partial melting of asthenosphere while thermal lithospheric mantle exists as undepleted asthenospheric mantle that cools to a semirigid viscosity.

The western US is an ideal region to examine the short-term evolution of plate boundaries because of its recent shift from a subduction-dominated to a transform tectonic environment and the availability of high-quality EarthScope Transportable Array seismic data. We utilize these data to produce new images of the regional Great Basin crust and upper mantle. By melding the broader regional tectonic history and the detail revealed by these images, we propose that both chemical and thermal lithosphere previously existed across much of Precambrian North America but that much of the thermal lithosphere beneath the Great Basin has been subsequently weakened and removed piecemeal as the Farallon slab rolled back and a slab window opened beneath the southwestern United States. Geologic and geophysical observations from the Great Basin suggest that the locations of thinnest lithosphere correlate with modern extension, volcanism, and

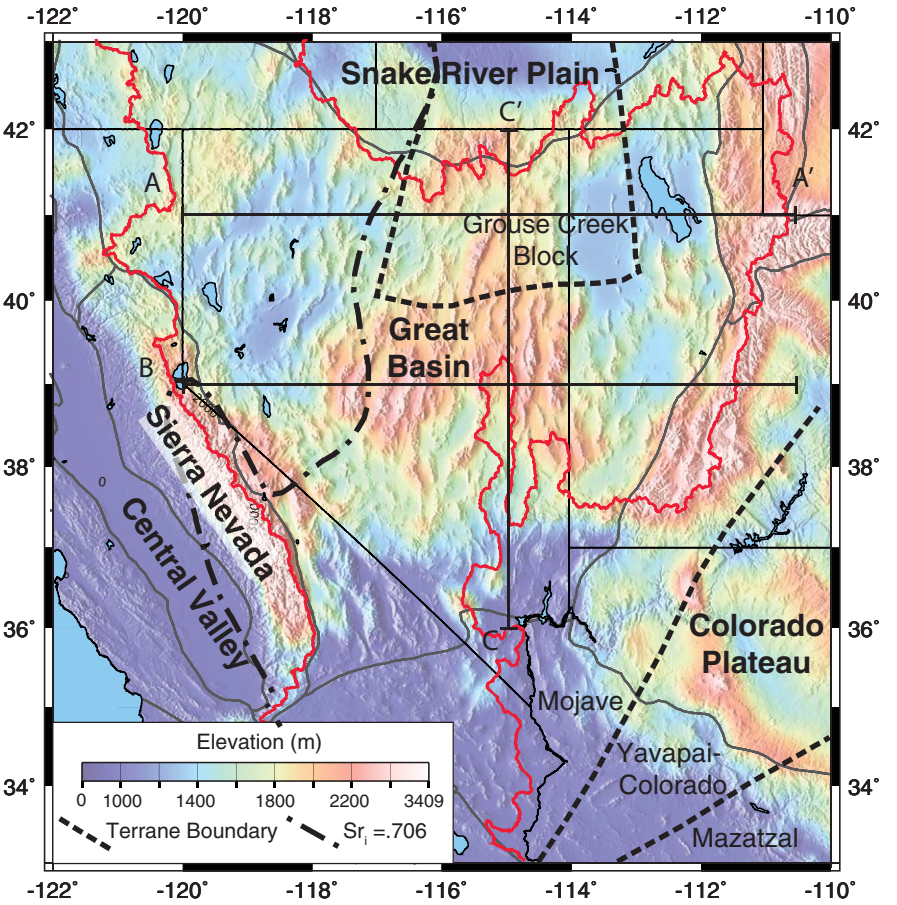

Figure 1. Map of filtered topography, physiographic provinces, and major terrane boundaries. The Great Basin, as defined hydrologically, is outlined in red, physiographic regions are outlined in gray, terrane boundaries and the $Sr_i = 0.706$ are black. Topography is low-pass filtered using a second-order Butterworth filter with half-weight at 70 km in order to highlight the long wavelength topography of the Great Basin. Terrane boundaries from *Mueller et al*. [2011]. Grouse Creek block from *Foster et al*. [2006]. $Sr_i = 0.706$ line from *DeCelles* [2004, and references therein].

seismicity. This, in turn, suggests that the geometry and strength of the lithospheric mantle play an important role in controlling the timing, nature, and magnitude of crustal deformation.

2. Geologic Background

The Great Basin is a highly extended region of the western US surrounded to the east and west by the relatively unextended Colorado Plateau and Sierra Nevada Mountains (Figure 1). The region's crust is composed of the Mojave terrane, a 2.6–1.6 Ga block of deformed crust that encompasses a majority of the Great Basin [*Mueller et al*., 2011; *Whitmeyer and Karlstrom*, 2007], and the Grouse Creek block, a >2.5 Ga block of cratonic rock that lies astride the northern Utah/Nevada border (Figure 1). The $^{87}Sr/^{86}Sr = 0.706$ line (Figure 1), which demarcates the western edge of Precambrian North America, is located west of the Grouse Creek block and runs north-south through the central the Great Basin suggesting a major lithospheric boundary within the region [*Kistler and Peterman*, 1978].

For much of the late Mesozoic and early Cenozoic, the Great Basin is believed to have existed as a high orogenic plateau, similar to the Tibetan and Iran-Turkish Plateau [*Dilek and Moores*, 1999]. This plateau, often termed the "Nevadaplano" [*DeCelles*, 2004], formed due to thin-skinned shortening along the western margin of north America caused by the collision of the Farallon and North American Plates. As plate geometries evolved, the Great Basin transitioned from a compressional to an extensional stress regime. Extension within the Great Basin is often divided into two phases, differentiated by time and style of deformation. The first phase began during Eocene time and is associated with slab rollback and the relaxation of the

overthickened crust that supported the Nevadaplano [*Coney and Harms*, 1984]. Core complex formation typifies deformation during this period [*Dickinson*, 2002, 2006]. The second extensional phase began ~18–16 Ma [e.g., *Noble*, 1972] and was driven by a reorganization of the Pacific-Farallon-North American plate margin from a subduction to a transform environment. This deformation, often referred to as "Basin and Range style" extension, is characterized by angular unconformities, magmatism associated with extension, and the development of the topography observed within the region today [*Zoback et al*., 1981].

There is significant variation in the structure and topography of the Basin and Range from north to south, with the Great Basin having the thinnest crust and highest heat flow of the province [*Sonder and Jones*, 1999]. The central Great Basin, a large internally drained region located primarily within the Northern Basin and Range (Figure 1), stands out from the surrounding regions in terms of topography, volcanic activity, seismicity, and mantle structure (Figures 1 and 2). This area has the highest elevations within the entire Basin and Range, with smoothed elevations ~400–500 m higher (Figure 1) than the Colorado Plateau and crustal thicknesses that are 5–15 km thinner. Gravity modeling shows that crustal thickness cannot account these high elevations suggesting that the topography must be supported by dynamic processes in the mantle [*Saltus and Thompson*, 1995]. The central Great Basin also exhibits less historic seismicity than the margin of the Great Basin [*USGS PDE Catalog (1973-Present)*], reduced heat flow ($<$60 mW/m^2) [*Blackwell and Richards*, 2004], and, with the exception of the ~400 km^2 monogenetic Lunar Crater volcanic field which first erupted ~4.2 Ma, has little volcanism younger than 30 Ma [*Best and Christiansen*, 1991] (Figure 2). These attributes suggest that modern strain in the region is concentrated along the margins of the Great Basin and that its interior is not deforming at present. Regional surface velocity fields determined by GPS corroborate this notion, and suggest that the central Great Basin is currently behaving as a rigid microplate with stress accommodated along its margins [*Bennett et al*., 2003]. Previous receiver function results suggest thinner crust and lithosphere along the eastern margin of the Great Basin [*Gilbert*, 2012; *Levander and Miller*, 2012; *Zandt et al*., 1995] as do magnetotelluric measurements [*Wannamaker et al*., 2008], consistent with the margins accommodating most of the strain within the region.

Late-Cretaceous and Cenozoic volcanism within the Great Basin can be divided into two phases. The first occurred prior to 18 Ma and is part of two concurrent time-transgressive sweeps of volcanism, referred to as the Ignimbrite Flare Up that began between 55 and 40 Ma and coalesced in southern Nevada ~20 Ma (Figure 2). The first sweep migrated southward from modern day southern Idaho while the second migrated northwest from southwest New Mexico [*Armstrong and Ward*, 1991; *Coney and Reynolds*, 1977; *Humphreys*, 1995]. These volcanic trends are characterized by large-volume silicic ignimbrite deposits, $>$70,000 km^3 of which were deposited in the southern Great Basin alone [*Best et al*., 2013], and were driven by the shallowing and subsequent rollback and foundering of the Farallon slab beneath the western US [*Armstrong and Ward*, 1991; *Humphreys*, 1995] (Figure 2a). From 20 to 17 Ma, there was a brief period of volcanic quiescence in the region (Figure 2b) [*McKee et al*., 1970], followed by the second phase of volcanism which continues today. This more recent volcanic activity is primarily basaltic in composition, focuses along the margins of the Great Basin [*Christiansen and McKee*, 1978], and is associated with Basin and Range extension and the opening of a slab window beneath the southwestern United States (Figure 2).

From a seismic imaging standpoint, the crust and upper mantle within the central Great Basin appears anomalous compared to the rest of the Basin and Range. In the upper ~150 km, a joint ambient-noise, earthquake-generated surface wave, and receiver function inversion shows thin crust (30–35 km) and a weak relatively high velocity feature extending down from the base of the crust to ~80 km depth within the upper mantle [*Shen et al*., 2013]. Similar features are observed within the upper mantle in tomographic images using both earthquake-generated surface waves [*Pollitz and Snoke*, 2010] and Pn phases [*Buehler and Shearer*, 2010]. Further, Sp receiver function images show variable lithospheric thickness within the Great Basin, with the thinnest lithosphere observed in the eastern Great Basin and thicker lithosphere observed in the central and western parts of the region [*Levander and Miller*, 2012].

Deeper within the mantle, a high-velocity anomaly is observed at ~190 km depth beneath the central Great Basin that extends down and connects to a large high-velocity body interpreted as Farallon slab remnants [*Schmandt and Humphreys*, 2010] (Figure 3). At this depth, relatively low velocities are observed along the margins of the Great Basin. While initial images of the upper-mantle high velocity features suggested that the high P-wave and S-wave velocities associated with this features were as fast as the Juan de Fuca slab where it is imaged clearly in the northern and southern Cascades [*Roth et al*., 2008; *West et al*., 2009],

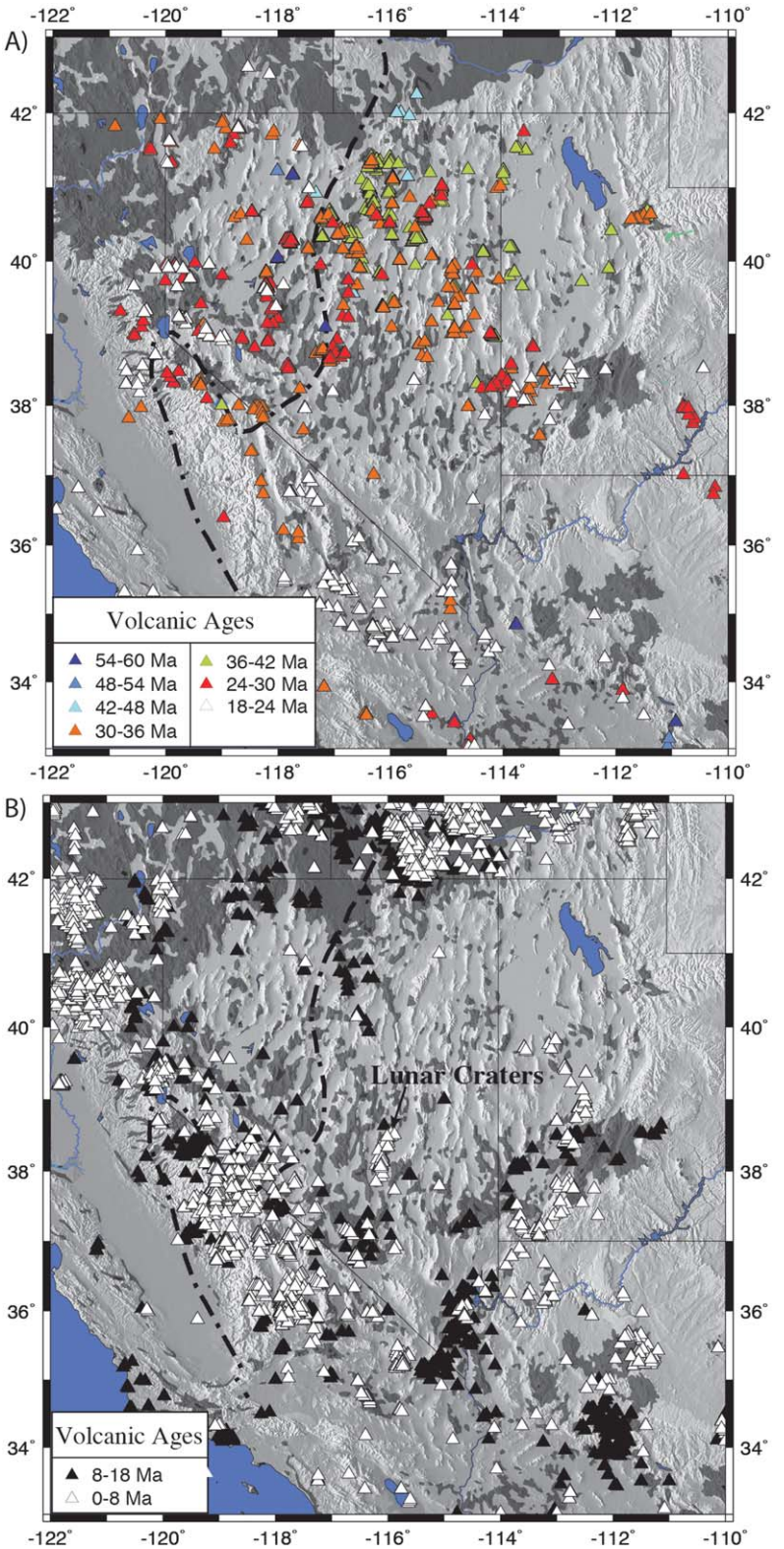

Figure 2. Maps of volcanic rocks for the Great Basin and surrounding region. Triangles are volcanic ages from the NAVDAT database (North American Volcanic Database, http://www.navdat.org/). Shaded areas are volcanic rock exposure from *Schruben et al.* [1994] and the dashed line is the $Sr_i = 0.706$ isopleth. (a) Older volcanism related to the ignimbrite flare up, which deposited volcanic rock throughout the northern Great Basin. Coloring in Figure 2a highlights the southward progression of volcanism during this period; (b) Recent volcanism associated with Basin and Range extension. The most recent volcanism (shown in white) concentrates almost exclusively at the margins of the Great Basin, with the exception of Lunar Craters volcanic field.

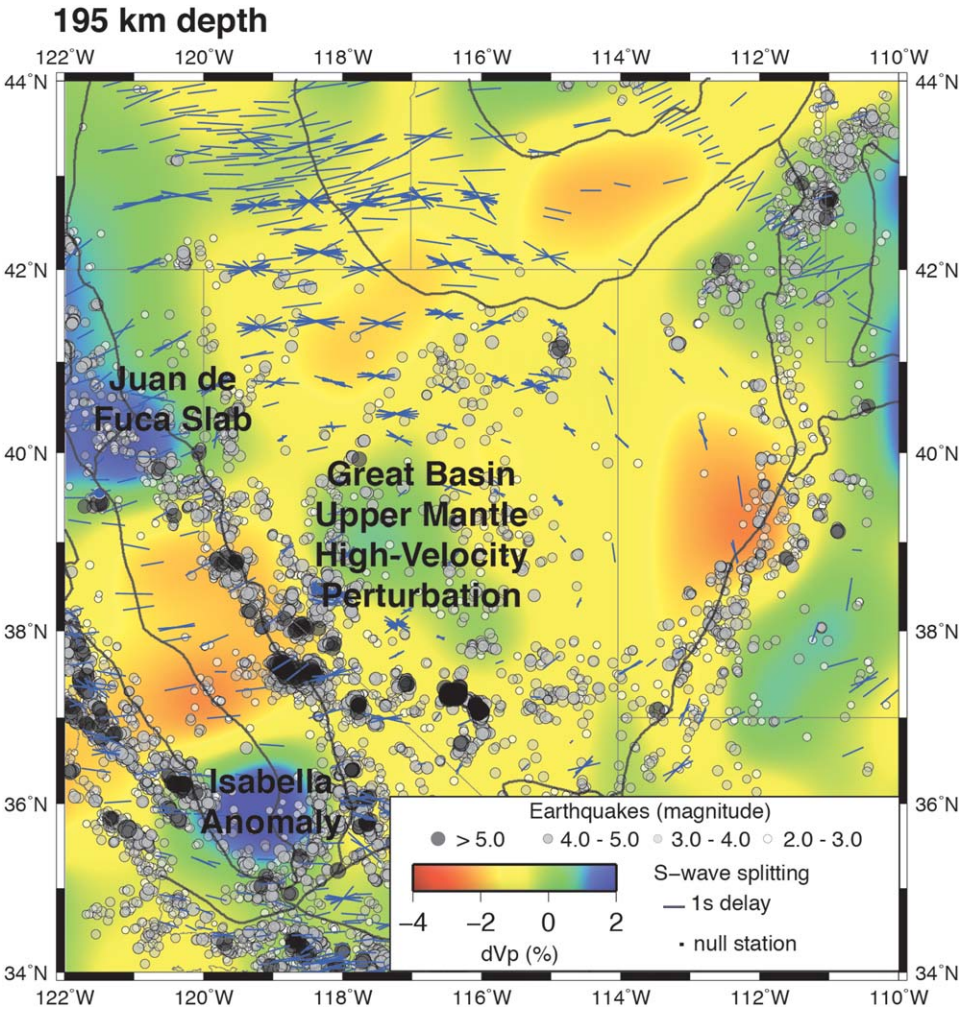

Figure 3. Map of P-wave velocity perturbations at 195 km depth, seismicity, and SKS splitting measurements from the Great Basin and surrounding regions. Map was created using the IRIS Earth Model Collaboration [*Trabant et al*., 2012] with tomography from *Schmandt and Humphreys* [2010], seismicity is from the USGS PDE Catalog 1973-Present, and SKS splitting measurement from *Wüstefeld et al*. [2009].

subsequent work suggests that the amplitude of this anomaly is much smaller [*James et al*., 2011; *Obrebski et al*., 2011; *Schmandt and Humphreys*, 2010; *Sigloch*, 2011]. Perhaps the most unusual seismic observation from the Great Basin is in the SK(K)S splitting measurements which show a circular pattern of anisotropy surrounding the Great Basin and the smallest splitting delay times observed in western US [*Savage and Sheehan*, 2000; *West et al*., 2009; *Yuan and Romanowicz*, 2010a; *Zandt and Humphreys*, 2008] within its center (Figure 3). Surface wave tomography also shows complicated patterns of anisotropy and suggests that multiple anisotropic layers in the crust and upper mantle are necessary to explain the regional anisotropic signal [*Lin et al*., 2010].

Based on this broad range of geophysical and geological observations, several hypotheses have been proposed to explain the upper mantle seismic observations from within the region. One is a model of toroidal flow, driven by the rollback of the Farallon slab [*Zandt and Humphreys*, 2008], which can explain the circular pattern of anisotropy orientations observed in the region. However, the toroidal flow model implies that strains of near zero exist in the center of the toroid, suggesting that older mantle fabric developed during Farallon subduction would still be intact. It remains a challenge to reconcile this issue with the weak shear-wave splitting observed within the center of the Great Basin without a resetting of the central Great Basin mantle fabric, possibly due to vertical mantle flow. An alternate explanation for this circular anisotropic pattern is that it is the result of the depth-integrated effects of differing anisotropic fabrics within the upper

mantle [*Yuan and Romanowicz*, 2010a]. These fabrics are hypothesized to relate to lithosphere-asthenosphere interactions in the upper 200 km and vertical flow associated with the underlying subduction of the East Pacific Rise. Another possibility that can explain these observations is one of large scale, modern, gravitationally driven removal of lithospheric material beneath the Great Basin [*West et al*., 2009]. In this scenario, the higher velocity material, interpreted as sinking lithosphere, generates vertical flow within the upper mantle and the weak anisotropic fabric observed in SK(K)S splitting measurements develops from vertical mantle flow that disrupts any pre-existing horizontal mantle fabric [*West et al*., 2009]. Finally, it is not fully possible to eliminate the possibility that the high-velocity feature observed in body-wave tomography is an artifact of body-wave tomographic inversions as a result of vertical smearing of Farallon slab remnants of the trapped at the 410 discontinuity [*James et al*., 2011; *Obrebski et al*., 2011; *Schmandt and Humphreys*, 2010]. While this possibility can explain the relatively low-amplitude high-velocity perturbation of this feature relative to the subducting Juan de Fuca slab and other presumed downwellings within the western US, it seems unlikely given that relatively higher velocities are evident in almost all of the tomographic images of the region. Further, it does not provide an explanation for the low-shear wave splitting times observed within the central Great Basin.

3. Methods

Using data from the EarthScope USArray Transportable Array and other stations available from the IRIS DMC, we present new surface-wave tomography and receiver function results to provide constraints on regional crust and uppermost mantle structure that allow us to test the competing models of Great Basin tectonics listed above. These analyses are done independently, allowing for us to compare results between the two methods and further constrain crustal and upper mantle structure.

For the receiver function analysis, we calculated Ps receiver functions at 265 stations within the Great Basin and surrounding region using an iterative time-domain deconvolution technique [*Ligorria and Ammon*, 1999]. Using the Standing Order for Data (SOD) software [*Owens et al*., 2004], we downloaded all events greater than magnitude 5.4 and 25°–95° distant from publicly available regional seismic stations deployed from 1994 to 2011. A total of 43,544 receiver functions from 2231 events were calculated from this data set. Due to the large size of this data set, we utilized automated quality control scripts to remove receiver functions unlikely representative of the Earth's structure, receiver functions with low-variance reduction ($<$80% on the radial components and $<$60% on the tangential component) and negative initial arrivals were discarded. The H-K stacking methodology of [*Zhu and Kanamori*, 2000] was used to estimate the crustal thickness and Vp/Vs ratio stations that recorded $>$10 events within the Great Basin. We used a bootstrapping method with 100 random resamples of each H-K stack to quantify the error in each station and discarded those stations with standard deviations $>$0.05 for Vp/Vs and 3 km for crustal thickness. The remaining H-K plots were then visually analyzed and those with ambiguous results (e.g., multiple amplitude peaks due to basin reverberations) were not further analyzed. Of the initial 265 stations, 89 were used for the final H-K stacks. Cross sections of receiver functions were created using common conversion point (CCP) stacks for all stations and within the data set that met the initial criteria [*Dueker and Sheehan*, 1997; *Gilbert et al*., 2003] with a bin size of 40 km. A Vp/Vs ration of 1.78 was used to migrate to depth in the CCP stack, which is based on the average from the H-K stacks. For CCP stacks, a Vp of 6.4 km/s was assumed for the upper 40 km and 8 km/s for greater depths.

For the surface wave analysis, we inverted Rayleigh wave phase velocity dispersion curves calculated from both the ambient-noise field and from earthquake-generated surface waves to produce a three-dimensional shear-velocity model for the region. By combining both ambient noise and earthquake-generated surface waves, we are able to calculate a shear-velocity model for a much larger depth range than either method allows individually. Ambient noise tomography [*Shapiro et al*., 2005] was used to calculate phase velocities between stations pairs at periods ranging from 8 to 40 s using the method outlined in *Bensen et al*. [2007]. Data from all publicly available stations in the region from 2005 to 2011 were used for an initial total of 29,752 cross correlations. Interstation phase velocities were utilized to calculate two-dimensional grids of phase velocity using the inversion technique described in *Barmin et al*. [2001]. The damping of the inversion is dependent on the path density with variables controlling the strength of the spatial smoothing, how data is merged into areas of poor data coverage and is the length of smoothing. In this step, cross correlations with signal-to-noise ratios of $<$15, those that were calculated from stations $<$3

wavelengths apart, and those that produced residuals >2 s in the phase-velocity grid inversion were not further analyzed. Resolution for the ambient noise measurements was calculated for the phase velocity maps and regions with resolution lengths worse than 100 km were not included in the shear-velocity inversion. Resolution was defined as the distance at which two δ-shaped functions can be differentiated from each other.

A two-plane wave approximation of earthquake-generated surface waves was used to measure phase velocities between 20 and 100 s [*Forsyth et al*., 1998]. This method has improved accounting for multipathing and perturbations to the wavefront over more traditional single plane-wave approaches. For the two-plane wave portion of the study, we utilized 77 earthquakes occurring from 2006 to 2009 with an epicentral distance of 30° to 130°. Two-plane wave measurements were smoothed using a Gaussian smoothing filter with a width of 75 km. Error within the two-plane wave inversion was quantified by calculating the standard deviation of phase velocity measurements; the entire study area fell within a standard deviation of 0.06. Dispersion curves from each method were combined and averaged for periods, where measurements were made with both techniques in order to utilize both data sets at those periods. Phase velocities were generally within 0.06 km/s of each other for results from the two techniques. At the 40 s period, the average misfit between the two methods was 0.058 km/s with a standard deviation of 0.056 km/s, at the 20 s period the average misfit was 0.061 with a standard deviation of 0.056.

The composite ambient-noise and earthquake-generated dispersion curves were inverted for shear velocity at grid points located every 0.1° using an iterative linearized least-squares inversion [*Herrmann*, 1987; *Snoke and James*, 1997; *Warren et al*., 2008]. In the starting model for the shear-velocity inversion, a Vs of 4 km/s and a Vp of 7 km/s were used, no Moho depths or other variations in velocity were prescribed to prevent us from biasing our results. Both P and S wave velocities were allowed to vary in the inversion but the Vp/Vs ratio was kept fixed, due to surface waves' low sensitivity to P-wave velocities. Sensitivity kernels based on the starting velocity model suggest resolution down to ~160 km depth. A more detailed description of the surface wave inversion and combination of ANT and two-plane wave dispersion curves can be found in *Porter et al*. [2012].

4. Results

4.1. Crustal Observations

In our analyses, we observe significant variations in crustal velocities, Vp/Vs ratios, and Moho depth across the Great Basin that appear to correlate well with seismicity and volcanism. Lateral variations in crustal shear velocities are best observed in map view (Figure 4). Depth slices from the upper/middle crust (Figure 4a) likely reflect upper crustal geology. In this image of the upper crust, lower shear velocities are observed in the Great Basin relative to the Colorado Plateau and Sierra Nevada Mountains as observed in previous studies [e.g., *Moschetti et al*., 2010; *Obrebski et al*., 2011; *Pollitz and Snoke*, 2010]. The lowest Great Basin shear velocities are observed at its eastern and western margins, where modern deformation concentrates. A weak high-velocity zone is observed in a north-south trending swath along the Utah-Nevada border, which correlates roughly with the location of lower-Paleozoic rock outcrops and the Grouse Creek block. This velocity pattern continues to the midcrust (Figure 4b), where the high-velocity feature is still imaged. Low-velocities in this midcrustal layer concentrate along the margins of the Great Basin and in a North-South running region defined by the $^{87}Sr/^{86}Sr = 0.706$ line (Figure 4). The low velocities in the vicinity of this line are consistent with this feature representing a significant lithospheric weakness dating to continental accretion. The midcrustal shear-velocity pattern largely extends down to the lower crust (Figure 4c) though amplitudes vary slightly. In this layer, it is likely that velocities are influenced by Moho structure, as surface wave inversions will often smear sharp velocity contrasts. The impact of the Moho velocity discontinuity likely extends to the 30–32 km depth layer (Figure 4d), where velocities largely reflect crustal thickness. At this depth, faster velocities are observed where the thinnest crust is imaged in receiver functions, consistent with lower crustal and mantle rock at these depths while lower velocities are consistent with crustal rock and thicker crust.

By stacking primary arrival and reverberations reflected off the surface of the Earth and back from the Moho, H-K analyses of receiver functions allow us to determine crustal thickness and the Vp/Vs ratio beneath each station (Figure 5 and Table 1). In our results, the Great Basin has thinner crust than the surrounding regions with estimated crustal thicknesses ranging from ~26 to 42 km. For the 66 stations located

within the Great Basin that were used for the H-K analysis, the mean calculated crustal thickness is 33.0 km with a standard deviation of 3.48 km. The mean Vp/Vs ratio for these stations is 1.78 with a standard deviation of 0.079. The overall pattern of Vp/Vs ratios is similar to that of *Lowry and Pérez-Gussinyé* 2011 though they observe a north–south band of high-Vp/Vs west of the $^{87}Sr/^{86}Sr = 0.706$ line instead of directly beneath it as we do. The thinnest crust is observed in the northern Great Basin, while a band of thicker crust is observed in the central Great Basin where higher elevations are found (Figure 1). These thicknesses agree with previous estimates made using TA data for the whole western North America [*Gilbert*, 2012], are broadly consistent with previous results from *Lowry and Pérez-Gussinyé* 2011 made using a filtering algorithm of EARS (EarthScope Automated Receiver Survey) data [*Owens et al*., 2004], as well as, with a study that jointly inverted receiver functions, ambient noise, and earthquake-generated surface wave data [*Shen et al*., 2013]. Variations that exist between this data set and EARS results likely relate to our removal of stations with significant basin effects, which were retained in other studies.

Vp/Vs ratios calculated from H-K stacks vary dramatically within the Great Basin and correlate both with tectonic blocks and recent deformation (Figure 5). Low Vp/Vs ratios are observed in the Grouse Creek Block and the western Great Basin, while higher Vp/Vs ratios are observed along the $^{87}Sr/^{86}Sr = 0.706$ line, the southeastern Great Basin, and the Colorado Plateau (Figure 5). With the exception of the western Great Basin, it appears that Vp/Vs ratios are well correlated with recent volcanism, as higher Vp/Vs ratios may represent fluid, partial melt, or increased temperatures, all of which can be associated with volcanism. However, as Vp/Vs ratios correlate well with tectonic blocks, it is unclear as to which factor is dominant in controlling the Vp/Vs ratios for the region.

Receiver functions and surface-wave tomography utilize disparate portions of the seismic signal, including seismic frequency ranges, and propagation paths of the seismic wavefield, both responding differently to variations in subsurface velocity. When similar features are observed in each data set, it provides compelling evidence for the robustness of the detected feature(s). Results from receiver functions and the surface wave inversion in this study image comparable structures across both data sets. In the surface wave inversion, the Moho depth was interpreted at the shallowest 4.2 km/s contour, while in CCP images it was interpreted as the most prominent conversion between 25 and 40 km depth (Figure 6). The Moho depths calculated by the two methods are largely consistent, though minor variations do exist. These variations are likely attributed to either high-velocity lower crust or low-velocity upper mantle that obscures the Moho (e.g., Figure 6b-b′, at 119°W). Overall, both methods suggest thinner crust in the northern and southern Great Basin separated by a region of thicker crust in the middle. In shear-velocity maps (Figure 4d), this is indicated by higher velocities in the north and south separated by a region of lower velocities. Though surface-wave velocities have a low sensitivity to P wave velocity and the Vp/Vs ratio, it is notable that in the 14–16 km depth section (Figure 4) the lowest shear velocities correspond to the regions of highest Vp/Vs, suggesting that the increased Vp/Vs is possibly a result of a drop in shear velocity.

4.2. Mantle Lithosphere

Within the uppermost mantle, we detect a ~6–10% decrease in shear-wave velocity in surface wave tomographic images that we associate with the lithosphere-asthenosphere boundary (LAB); this feature is best identified in cross section (Figure 6). A clear LAB conversion is not observed in the Ps receiver function images, owing to reverberations from the Moho interfering with conversion. Shear velocities show LAB depths that vary across the Great Basin from ~80 km in the center to <50 km at the eastern margin (Figure 2). The thickest lithosphere in the Great Basin is located within its center and is collocated with the area of reduced seismicity and volcanism (Figures 4 and 5). Both the presence of a distinct LAB signal underlying the central Great Basin and the decrease in seismic velocity with respect to depth throughout the Great Basin indicate that the deeper high-velocity column imaged by body-wave studies is physically detached from the shallower lithospheric structure. A high-velocity feature in the central Great Basin is imaged in map view in the 55–60 km and 70–75 km depth layers immediately east of the $^{87}Sr/^{86}Sr = 0.706$, which demarks the western edge of Precambrian North America (Figure 4), and is representative of the lithospheric root seen in cross section (Figure 6). This observation is confirmed in both EW cross sections that show the thinnest lithosphere at the $^{87}Sr/^{86}Sr = 0.706$ line and at the margins of the Great Basin, further suggesting this boundary to be a lithospheric scale weakness that is being exploited by extensional deformation. It is also notable that the volcanism and seismicity as well as increased Vp/Vs ratios (Figure 5) are observed immediately above the thinnest lithosphere. In the north-south cross section, the thickest

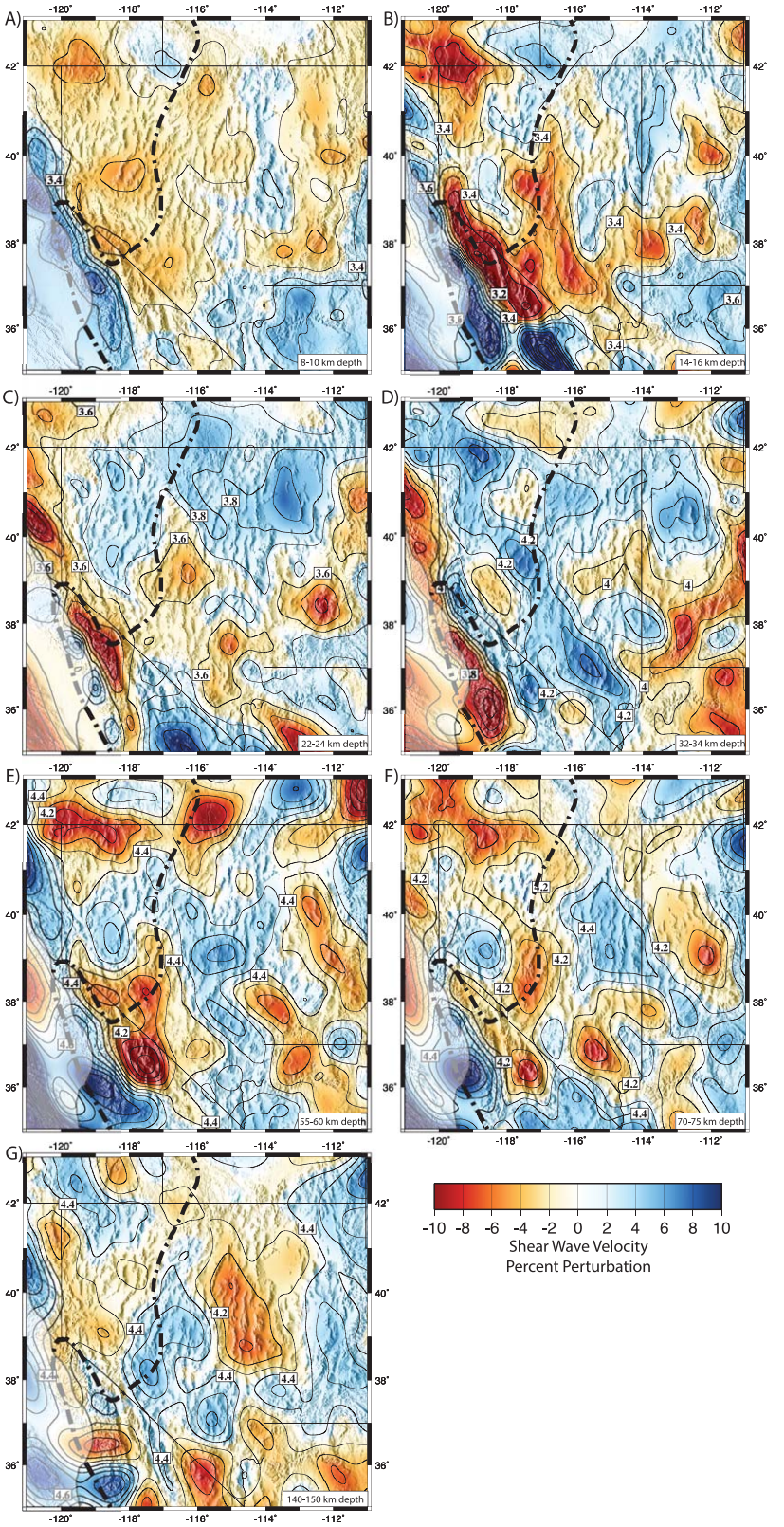

Figure 4. Map views of shear velocity perturbations for the Great Basin region at crustal and upper mantle depths. Contours give absolute velocities in km/s. The shaded out regions in southwestern part of the plot are the areas with worse than 100 km resolution in ANT measurements at the 40 s period. Two plane-wave measurements have resolution throughout the study area. Dashed line is $^{87}Sr/^{86}Sr = 0.706$ isopleth.

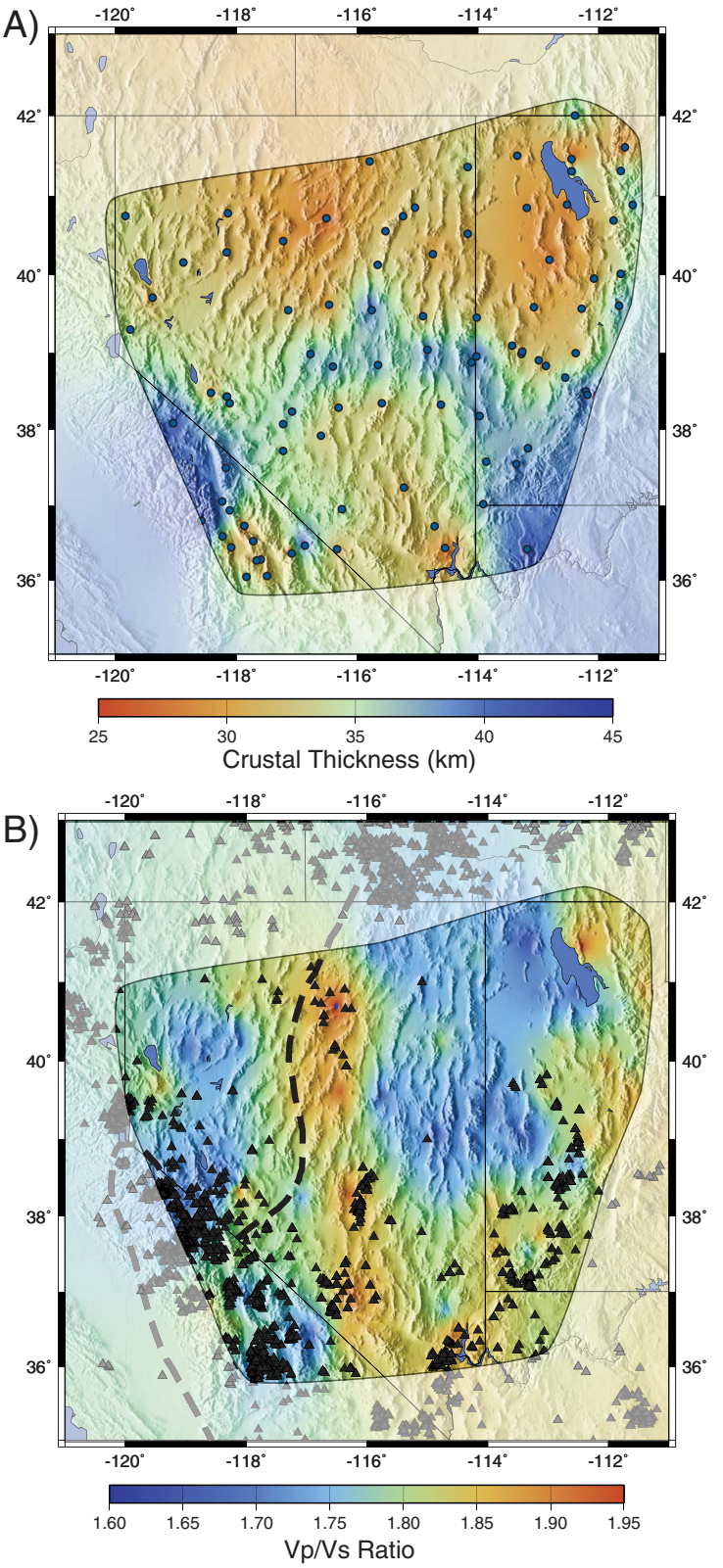

Figure 5. (a) Map of crustal thickness and (b) map of Vp/Vs ratios calculated using tension-based gridding of HK stacks. Station locations are shown by blue circles in Figure5a. Colors are interpolated between stations. Gray triangles are recent (<18 Ma) points from the NAVDAT database. Dashed line is $^{87}Sr/^{86}Sr = 0.706$ isopleth.

lithosphere is observed between 40° and 41° North, where the Grouse Creek Block is observed (Figure 6). The lithosphere thins north of 41° which is reasonably attributed to lithospheric modification/thinning caused by heating along the Yellowstone hotspot track. Calculations of lithospheric thickness from Ps and Sp receiver functions show significant variability in the depth of the LAB across this region. Thinned lithosphere is observed along the eastern margin of the Great Basin and a deeper LAB is imaged where we detect a lithospheric root [*Levander and Miller*, 2012]. However, these receiver function measurements show relatively thick lithosphere in the southwestern Great Basin where our tomographic images suggest thinner lithosphere. This difference in LAB depths could result from the hypothesized mantle convection in the southern Sierras [e.g., *Zandt*, 2003]. In the 140–150 km depth layer, the high-velocity feature observed in our surface-wave inversion (Figure 4g) correlates with the location of the high-velocity feature observed in body-wave tomography in the southwestern Great Basin. In both body-wave and surface-wave images, this feature is found below a region of thin lithosphere and adjacent to the thickened lithospheric root observed in our surface-wave tomography. Based on its depth and location, we argue that this high-velocity feature as potentially representative of small pieces of mantle lithosphere that have destabilized and sunk into the underlying asthenosphere as extension occurred within the region, though it falls near the edge of our model and cannot be well constrained.

5. Discussion

Any model to explain the region's tectonics must be able to explain the following observations: (a) the presence of a relatively high velocity perturbation in the upper asthenosphere in body-wave tomography, (b) the absence of significant upper mantle seismic anisotropy observed in SKS splitting, (c) the focusing of recent seismicity, volcanism, and extension along the margins of the Great Basin, (d) the high elevations and relatively thin crust observed within the central Great Basin, (e) variations in lithospheric thickness across the Great Basin, and (f) the relatively low Vp/Vs ratios observed within the center of the Great Basin in receiver function H-K stacks. Below we discuss existing hypotheses for crustal and mantle dynamics within the region and suggest a new model based on existing observations and our updated results.

Both upward [e.g., *Saltus and Thompson*, 1995] and downward [e.g., *West et al*., 2009] upper mantle flow have been hypothesized to explain geologic and geophysical observations within the Great Basin. There is little seismic evidence for a modern, focused, asthenospheric upwelling analogous to Yellowstone, beneath the Great Basin. It is more likely that the opening of the slab window beneath the region led to broad-scale upwelling of asthenosphere that weakened the overlying lithosphere and encouraged subsequent downward flow of cold lithospheric material. Recent work has shown that the amplitude of the high-velocity perturbation observed in the upper mantle near the proposed cold Great Basin downwellings are weaker than indicated in initial models, and significantly lower velocity than other hypothesized downwellings in the Western US, such as the southern Sierra [*Zandt*, 2003], Wallowa [*Hales et al*., 2005], and Colorado Plateau downwellings [*Levander et al*., 2011]. Based on the size and location of higher velocities in body-wave tomography models at ~400 km depth [*James et al*., 2011; *Obrebski et al*., 2011; *Schmandt and Humphreys*, 2010], this feature is more consistent with a stalled Farallon slab at 410 km depth than a lithospheric downwelling extending down 800 km as hypothesized in *West et al*. [2009].

If the high-velocity anomaly observed in body-wave tomography from ~150 to 350 km depth were a slab fragment, it must have remained largely undeformed and stationary beneath the Great Basin since the slab window was extensively developed beneath the region at 10 Ma or greater [*Dickinson and Snyder*, 1979] This scenario is inconsistent with the significant reworking of the mantle that occurred over the last 40 Ma, and adds to the challenge in explaining the regional SKS splitting low. Additionally, a cold and wet slab lacks the positive buoyancy necessary to anchor a fragment above the 410 km discontinuity [e.g., *Bina et al*., 2001].

Due to the high angle of incidence of the seismic waves used in teleseismic body-wave tomography, vertical smearing between nodes is common in both S-wave and P-wave inversions. For this reason, the relatively high-velocity perturbation observed in body-wave tomography could result in a structural artifact from the vertical smearing of the high-velocity 100 km thick lithosphere observed beneath the central Great Basin and Farallon Slab remnants trapped at the 410 km discontinuity [*James et al*., 2011; *Schmandt and Humphreys*, 2010]. If this feature were a tomographic artifact, it would explain the low amplitudes of this

Table 1. Station Names, Locations, Crustal Thicknesses, and Vp/Vs Ratios Calculated Using HK-Analysis

Station Name	Latitude	Longitude	Moho Depth (km)	Moho Std	Vp/Vs	Vp/Vs Std
A07	40.5576	−115.5263	32	1.858	1.78	0.047
BMN	40.4315	−117.2218	29	0.098	1.81	0.004
BVC	36.7266	−117.8633	30	1.705	1.77	0.045
CCUT	37.5506	−113.3627	39	2.062	1.76	0.041
CPR	36.7972	−118.5754	43	1.241	1.84	0.028
CTU	40.6925	−111.7503	32.5	0.144	1.77	0.007
CWC	36.4399	−118.0802	31.5	0.251	1.79	0.01
DAC	36.277	−117.5937	32.5	0.243	1.76	0.01
DP00	36.2646	−117.6601	32	1.43	1.78	0.043
DUG	40.195	−112.8133	28	0	1.83	0.003
ELK	40.7448	−115.2388	31.5	0.128	1.76	0.005
FUR	36.467	−116.8632	41	2.28	1.66	0.048
GAR	38.8808	−114.102	38	0.33	1.72	0.019
HFEB	36.3608	−117.0767	31.5	1.254	1.72	0.035
HWUT	41.6069	−111.5652	28	0.605	1.84	0.02
L15A	42.0041	−112.386	36.5	2.245	1.82	0.025
M11A	41.4311	−115.7912	30	2.447	1.7	0.047
M13A	41.3602	−114.1655	34.5	0.245	1.78	0.009
M14A	41.503	−113.3471	30	0.25	1.64	0.01
M15A	41.4632	−112.4477	26	0.292	1.96	0.012
M16A	41.3146	−111.6298	35.5	1.524	1.81	0.045
MNV	38.4328	−118.1531	37.5	0	1.75	0
MPM	36.058	−117.489	32	0	1.76	0
MPU	40.0155	−111.6333	35	0.246	1.78	0.005
MVU	38.5037	−112.2123	39	0.357	1.83	0.012
N06A	40.7484	−119.8346	34	0.151	1.78	0.009
N08A	40.7811	−118.1337	31.5	0.169	1.85	0.007
N10A	40.7186	−116.508	27	0.181	1.98	0.008
N12A	40.8522	−115.0387	33	0.232	1.73	0.017
N14A	40.8513	−113.1867	29	1.728	1.71	0.045
N15A	40.8903	−112.5201	28	0.533	1.64	0.015
N16A	40.8869	−111.437	36.5	0.542	1.87	0.016
NLU	39.9548	−112.075	30.5	0.944	1.86	0.03
NV31	38.4328	−118.153	37.5	0.275	1.75	0.006
NV33	38.485	−118.4183	31	0.131	1.66	0.008
NWC	38.9883	−116.768	37	2.646	1.84	0.048
O07A	40.1614	−118.8772	33	0.169	1.68	0.007
O08A	40.2903	−118.155	31.5	0.244	1.71	0.013
O11A	40.1313	−115.657	33	0.24	1.77	0.009
O12A	40.2679	−114.7454	30	0.321	1.8	0.01
P09A	39.5516	−117.1395	32	0.94	1.86	0.031
P10A	39.6202	−116.4639	29.5	0.992	1.94	0.036
P11A	39.553	−115.7536	40.5	1.545	1.68	0.032
P12A	39.4731	−114.9075	32	0.423	1.75	0.013
P13A	39.455	−114.0156	32	1.485	1.69	0.052
P14A	39.5906	−113.0687	30	0.251	1.83	0.01
P15A	39.5708	−112.2786	31.5	0.197	1.8	0.007
P16A	39.6092	−111.6595	37.5	0.468	1.87	0.011
PAH	39.7106	−119.3854	31.5	1.142	1.85	0.039
Q10A	38.8247	−116.3999	37.5	0.238	1.8	0.006
Q11A	38.8455	−115.6541	37.5	0.917	1.77	0.024
Q12A	39.04	−114.8299	39	0.098	1.68	0.004
Q13A	38.9551	−114.0202	40	0.288	1.76	0.009
Q14A	38.9882	−113.2769	33	0.206	1.68	0.006
Q15A	38.9995	−112.3793	31.5	0.442	1.86	0.013
R07C	38.089	−119.0469	41.5	0.409	1.68	0.009
R08A	38.3489	−118.1064	34.5	0.218	1.88	0.008
R09A	38.2397	−117.0718	36.5	0.248	1.74	0.009
R10A	38.2886	−116.3021	33	0.407	1.93	0.027
R11A	38.3489	−115.5854	32	0.317	1.8	0.01
R12A	38.3281	−114.6076	33.5	0.123	1.74	0.006
R13A	38.1802	−113.9691	38.5	1.133	1.86	0.029
S08C	37.4993	−118.1711	39	0.188	1.81	0.01
S09A	37.7243	−117.2246	35	2.869	1.8	0.027
S10A	37.923	−116.5948	32.5	0.136	1.83	0.006
S13A	37.5808	−113.8604	36	0.098	1.86	0.005
S14A	37.7601	−113.1684	37	0.391	1.86	0.017
SLC	36.5243	−117.7175	32.5	0.767	1.79	0.036

Table 1. (continued)

Station Name	Latitude	Longitude	Moho Depth (km)	Moho Std	Vp/Vs	Vp/Vs Std
SPU	41.3087	−112.4492	37	1.606	1.85	0.045
SRF	36.936	−118.1061	38	0.675	1.71	0.021
SUG00	36.0459	−117.8319	34.5	0.987	1.72	0.027
T11A	37.2408	−115.2202	31.5	0.195	1.81	0.008
T12A	36.7256	−114.7147	33	0.139	1.74	0.006
T13A	37.0195	−113.9073	37.5	0.272	1.84	0.013
TIN	37.0542	−118.2301	37.5	0.762	1.77	0.015
TPH	38.075	−117.2225	35.5	0.111	1.78	0.007
TPNV	36.9488	−116.2495	35.5	0.215	1.93	0.009
U10A	36.4193	−116.3297	31.5	0.428	1.87	0.014
U12A	36.4321	−114.5388	26	0.521	1.92	0.022
U14A	36.4182	−113.1805	42	0.123	1.8	0.006
UT64	38.457	−112.183	39.5	0.419	1.81	0.009
UT66	38.681	−112.552	37	0.605	1.7	0.015
UT68	38.833	−112.873	31.5	0.297	1.81	0.017
UT69	38.908	−112.991	32	0.247	1.77	0.011
UT70	39.017	−113.261	32	0.813	1.68	0.02
UT71	39.094	−113.43	32	1.228	1.68	0.022
WCN	39.3017	−119.7563	34.5	0	1.77	0.005
WCP	40.5242	−114.167	31.5	0.776	1.75	0.023
WHP	36.5888	−118.2229	35	0.372	1.82	0.014

central Great Basin high-velocity perturbation and why it connects to slab remnants at depth. While we cannot rule out this hypothesis, it does not explain the absence of significant SK(K)S splitting within the central Great Basin. Furthermore, the thickest lithosphere within the Great Basin is located adjacent and not above this body-wave mantle perturbation making vertical smearing between the two less likely.

Given our new images, we propose an alternative tectonic model that incorporates parts of the above hypotheses to explain the geologic and geophysical observations from the region in the context of its tectonic evolution (Figure 7). In our model, we suggest that thick lithosphere existed beneath the Great Basin prior to extension. Beneath Precambrian North America, this lithosphere consisted of depleted materials, forming a chemical lithosphere. As subduction ceased, a slab window opened up beneath the region, resulting in the attached thermal lithosphere destabilizing and fragments of thermal mantle lithosphere sinking into the upper mantle. This piecemeal downwelling of the lithosphere helped drive upper mantle convection at the margins of the Great Basin which brought hot asthenosphere into contact with preexisting lithospheric weaknesses, such as the $^{87}Sr/^{86}Sr = 0.706$ line, concentrating deformation in these regions and further thinning the lithosphere in these areas which, in turn, produced the modern topography we observe. This LAB topography is interpreted in light of recent work from the eastern North American craton that suggests cratonic mantle lithosphere consists of two separate layers; chemical and thermal lithosphere [*Griffin et al*., 2004; *Yuan and Romanowicz*, 2010b], which are differentiated by composition, age, and provenance.

The composition of subcontinental lithospheric mantle is largely determined by the degree of basaltic melt extraction, which, in turn, correlates well with the age of the crust. The lithospheric mantle beneath Phanerozoic crust is largely fertile while Archean crust is underlain by strongly depleted lithospheric mantle [*O'Reilly and Griffin*, 2006]. While Archean and Phanerozoic mantle lithospheres represent end members on the spectrum of melt-depletion, Proterozoic lithosphere is intermediate of the two, further, Archean mantle lithosphere can be refertilized due to metosomatism, making them less depleted than would be expected [*Griffin et al*., 2009]. In the following sections, we refer to chemical lithosphere as depleted subcontinental lithospheric mantle, commonly associated with cratonization [*Pollack*, 1986]. Within the Great Basin, this chemical lithosphere likely consists of Proterozoic or refertilized Archean lithosphere which is stronger and less dense than the underlying "thermal lithosphere" consisting of undepleted peridotite that has cooled sufficiently to behave rheologically as lithospheric material [*Griffin et al*., 2004; *Yuan and Romanowicz*, 2010b]. Though these two end-member lithosphere types exhibit similar seismic velocities [*Deschamps et al*., 2002], they can be distinguished by their buoyancy, strength and composition. Given its reduced density, chemical lithosphere is unlikely to become gravitationally unstable and descend into the underlying asthenosphere. A reasonable explanation for the thick root beneath the central Great Basin is that it consists of chemical lithosphere and is therefore positively buoyant and stable.

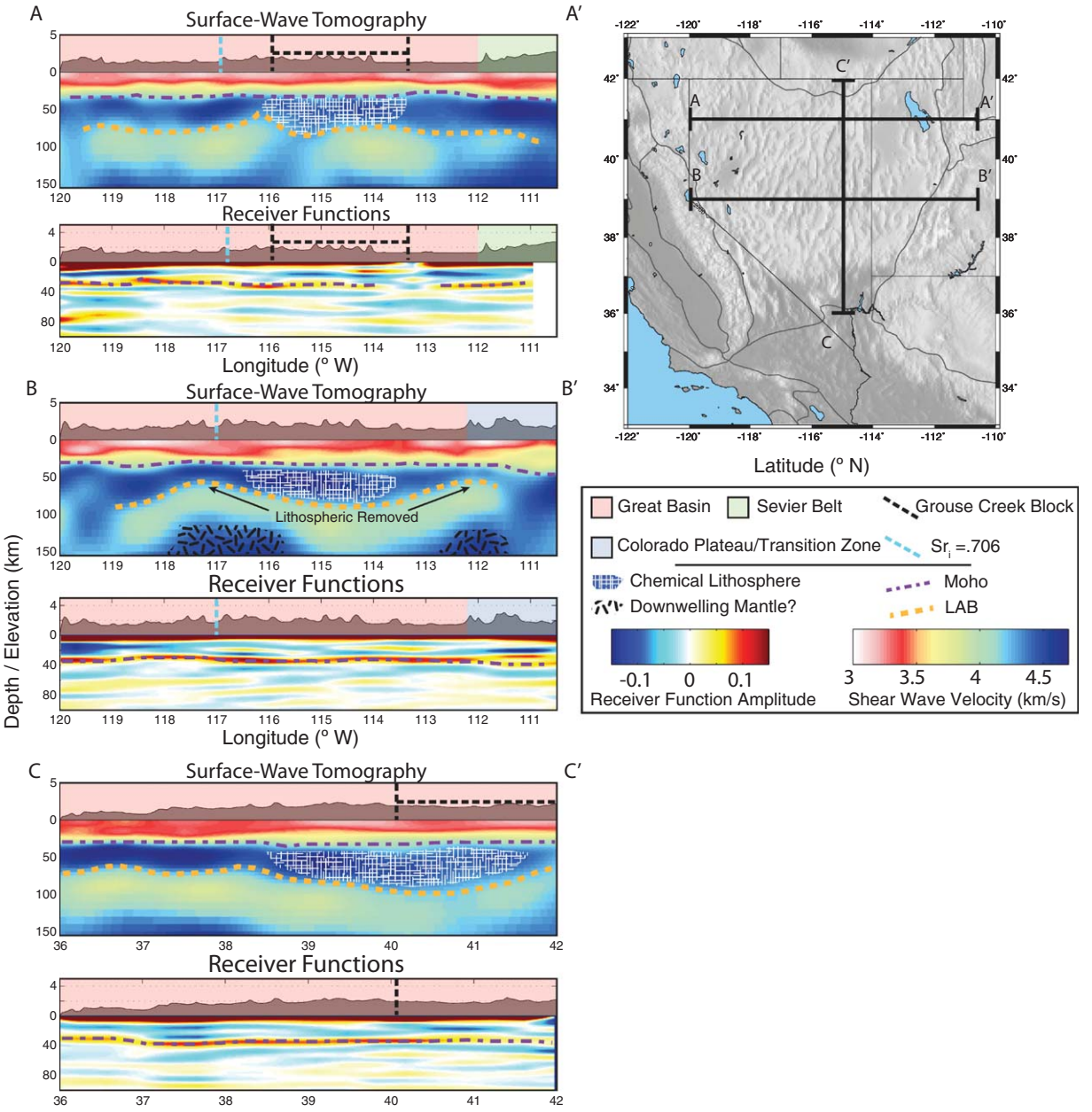

Figure 6. Cross sections of shear velocities and receiver function CCP stacks. Moho and LAB depths are interpreted from each image. Cross section locations (A-A′, B-B′, and C-C′) are shown on the map.

We suggest that the thick lithospheric root in the central Great Basin represents the largely intact chemical lithosphere of Precambrian North America, specifically the >2.5 Ga Grouse Creek block, which, at the surface, is located immediately above and slightly north of the observed higher velocity root [*Egger et al.*, 2003; *Foster et al.*, 2006] (Figure 1). The lithosphere associated with this cratonic block was presumably depleted to form chemical lithosphere during a partial melting event prior to continental accretion, this is consistent with magnetotelluric data that indicate a high-resistivity layer extending down to 150 km depth and interpreted as thickened lithosphere [*Bedrosian and Feucht*, 2013]. The Grouse Creek block represents the oldest crust within the Great Basin and lies immediately adjacent the $^{87}Sr/^{86}Sr = 0.706$ isopleth that defines the boundary of Precambrian North America. The crust lying west of the $^{87}Sr/^{86}Sr = 0.706$ line is considerably younger and is less likely to be underlain by a depleted chemical lithosphere while the crust to the east is part of the 2.0–1.7 Ga Mojave terrane [*Foster et al.*, 2006] and underlain by a smaller root of chemical

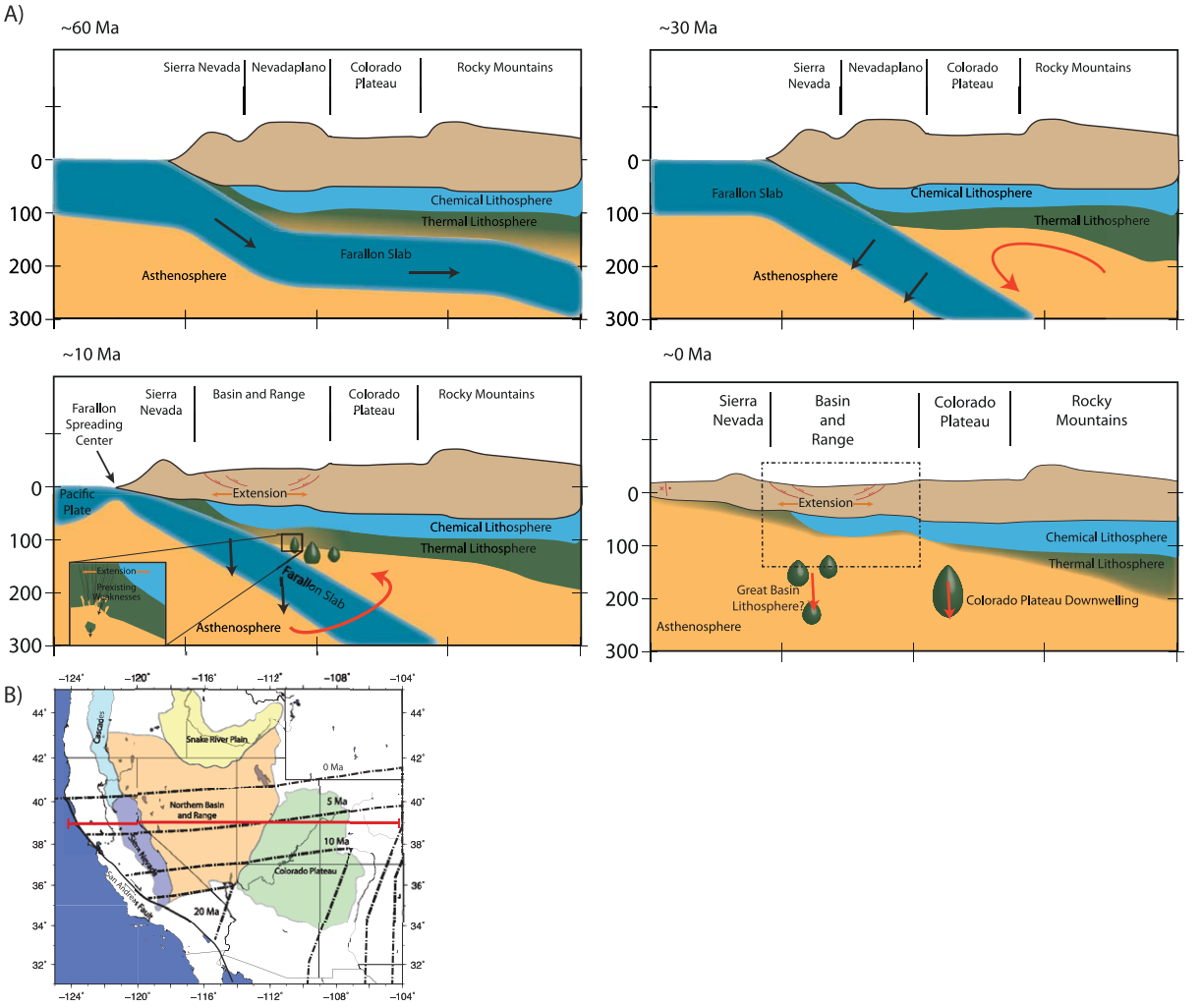

Figure 7. A) Cartoon diagram showing cross sectional views of our model of the recent tectonic evolution of the Great Basin. The inset in the 10 Ma cross section shows the piecemeal removal of thermal lithosphere. The dashed box in the 0 Ma cross section is the location of cross section B-B′ in Figure 6. In this image, the features labeled "Great Basin Lithosphere?" represent the high-velocity features at the bottom of our shear-velocity model. B) Map view showing the location of the cross section (red) and the opening of the slab window beneath the southwestern US through time (dashed line) [*Dickinson and Snyder*, 1979].

lithosphere. Though we cannot determine the difference between these two types of lithosphere based on seismic velocities, the correlation between lithospheric thickness, age, surface elevations, as well as the multiple layers of anisotropy necessary to explain surface wave observations [*Lin et al.*, 2010] suggest that this is a plausible explanation for these observations.

During the majority of the Cretaceous and early Tertiary time, the Great Basin existed as a high orogenic plateau, dominated by compression and thin-skinned shortening. During late Cretaceous/early Tertiary flat-slab subduction, the lithosphere beneath the Great Basin was hydrated/metasomatized by water released from the downgoing Farallon plate. As the slab rolled back to resume a more common subduction angle, hot asthenosphere came into contact with the slab-hydrated Basin and Range lithosphere, generating extensive partial melting and resulting in the ignimbrite flare-up [e.g., *Humphreys et al.*, 2003]. While volcanism was extensive throughout the region, forming several large volcanic fields and depositing large quantities of volcanic ash, it is notable that the volume of deposited volcanic material in geologic maps [*Best et al.*, 2013] is significantly reduced in the vicinity of thickened lithosphere. A root of chemical lithosphere would inhibit volcanic activity in these regions either by (1) thermally insulating the crust or (2) by preventing melt from penetrating to the surface (Figure 2). Interestingly, the only core complexes that formed in the central Great Basin are located in the region underlain by this root [e.g., *Dickinson*, 2002], perhaps indicating a relationship between core complex formation and the buoyancy of thickened chemical lithosphere.

Basin and Range style extension began ~16–18 Ma in the region and was caused by transtension due to the relative motion of the Pacific and North American plates and by thermal weakening of the lithosphere caused by upwelling asthenosphere as the slab window opened beneath the southwestern US. During this time, extension likely occurred throughout the lithospheric column, including both the crust and mantle lithosphere, though it is hypothesized that two likely decoupled and extended at different rates as suggested by modern GPS measurements, seismic observations, and geologic data [*Wernicke et al*., 2008]. Within the mantle lithosphere, Basin and Range style extension occurred along pre-existing lithospheric boundaries. For example, the thinnest modern lithosphere is observed along the $^{87}Sr/^{86}Sr = 0.706$ line and at the boundary between the Colorado Plateau and Great Basin, indicating that these zones may have been preexisting weaknesses prior to extension. As extension focused in these areas, hot asthenosphere and fluids intruding into the thermal lithosphere would have further concentrated extension and destabilized fragments of the thermal lithosphere. Models of lithospheric removal [e.g., *Elkins-Tanton*, 2005; *West et al*., 2009] show that downwellings significantly thin the lithosphere, consistent with seismic images of the Great Basin showing thin lithosphere in the locations where we hypothesize removal has occurred. Lithospheric downwelling would produce vertical flow within the mantle that would reset any previous horizontal anisotropy and, as such, can explain the weak SK(K)S splitting in the region. This idea of regional vertical flow has previously been proposed to explain observations of radial anisotropy beneath 150 km depth in the area [*Yuan et al*., 2011]. A downwelling that generated vertical mantle fabric would contribute to the high-velocity perturbation observed in body-wave tomography [e.g., *O'Driscoll et al*., 2011], and contribute to the upward smearing of the Farallon slab in these tomographic images. While we cannot constrain a precise date of the onset of lithospheric removal, it most likely occurred between the opening of the slab window at ~18 Ma and present. If the removal was recent, the high-velocity features are observed at ~150 km depth in our shear velocity model could represent these detached pieces (Figures 6 and 7) though further work is required to confirm this.

Modern GPS data [*Bennett et al*., 2003] demonstrate that Basin and Range style extension continues to the present, and is at least partially controlled by the structure of the mantle lithosphere. GPS measurements show that extension focuses at the edges of the Great Basin, where we image the thinnest lithosphere and concentrated zones of volcanism and seismicity (Figure 6). Heat flow is also reduced in the central Great Basin [*Blackwell and Richards*, 2004]. Heat from the opening of the slab window and slab-derived volatiles from the Farallon slab migrated upward into the lithosphere and helped enable modern extension and volcanism. The central Great Basin is thus at least partially insulated from this deformation by its thick root of chemical lithosphere. Furthermore, as previously hypothesized by *Humphreys and Dueker* [1994], this chemical lithospheric root potentially provides the buoyancy necessary to support the high elevations of the central Basin and Range. This is consistent with observations by *Becker et al*. [2013], which suggest that the difficulty in reconciling crustal structures and mantle flow inferred from tomography with regional topography, may stem from seismic anisotropy or from depletion of the upper mantle. Finally, the formation of this root through melt depletion and subsequent crustal melting would have led to further felsification of the crust in the central Great Basin. The high quartz content associated with crustal felsification would significantly reduce the Vp/Vs ratios [e.g., *Christensen*, 1996]. The low-Vp/Vs region of the central Great Basin correlates well with the location of the Grouse Creek block, composed largely of orthogneiss [*Egger et al*., 2003; *Foster et al*., 2006]. Alternatively, variations in crustal Vp/Vs could result from recent deformation, elevated temperatures, and/or fluid inclusions that have elevated the crustal Vp/Vs ratios away from the root at which deformation and volcanism are currently concentrated in the regions of thinnest lithosphere.

For lithospheric downwelling to occur, two requirements must be met, (1) a gravitationally instability must be produced and (2) this instability must destabilize so that it can sink into the asthenospheric mantle. Viable ways of producing a gravitational instability in the lithosphere include the formation of a dense mafic root during batholith formation, the cooling and densification of lithospheric mantle, and/or through phase changes, such as the basalt to ecologite transition that occurs within the crust of downgoing oceanic plates. Destabilization can occur through extension, entrainment by mantle flow, and the weakening of the lithospheric column through melting. Subduction and its cessation significantly alter the dynamics of the surrounding crust and mantle through the introduction of volatiles, the driving and alteration of mantle flow, and compression and subsequent relaxation of the lithosphere, all of which help produce the above conditions necessary for lithospheric downwelling to occur. While we further constrain the hypothesized downwelling occurring beneath the Great Basin by imaging crustal and upper mantle structure and introducing

the concept of chemical and thermal lithospheres to the region, we argue that lithospheric downwellings are common in postsubduction environments based on the numerous hypothesized downwelling in the western US [*Hales et al.*, 2005; *Levander et al.*, 2011; *Zandt*, 2003]. We also suggest that these downwellings are dependent upon preexisting crustal and upper mantle features such as lithospheric weaknesses and variability in depletion of the mantle-lithosphere. These downwellings are important in the thermal and chemical evolution of both the crust and lithospheric mantle and in focusing active deformation.

6. Conclusions

Based on a range of existing geologic and geophysical data and our new images of crustal and lithospheric structure, we present a revised model for the recent tectonic evolution of the Great Basin region of western North America. Our model is based on the idea that thermal and chemical lithosphere exists beneath parts of the Great Basin and that current structure is the result of the removal of the thermal lithosphere. This removal is controlled partially by pre-existing structures in the mantle lithosphere that date back to the formation of the North American continent. The downwelling and focused extension of the lithosphere produced vertical mantle flow and weakened the crust at the margins of the Great Basin; this is where increased extension, volcanism, seismicity, and heat flow are observed. In our dynamic scenario, the intact root of chemical lithosphere would inhibit volcanism, deformation, heat flow, and electrical conductivity, and support the high elevations in the central Great Basin.

The western US provides the type example of this concept due to its tectonic history and the availability of wide-aperture, high-quality seismic data; lithospheric erosion is expected to be a common feature of contemporaneous postsubduction environments. Further, the process of piecemeal thermal lithosphere erosion and removal would likely occur in regions outside subduction systems, such as those where subcrustal temperatures have increased through rifting, small-scale convection, and plume interactions [*Kerr*, 1994]. This process also likely plays a significant role in focusing deformation and volcanism, leading to the chemical evolution of continental crust. While the concept of coexisting thermal and mechanical lithosphere is important in explaining growth and evolution of cratonic lithosphere, we argue that it may be equally important in explaining the destruction of lithosphere in actively deforming regions.

Acknowledgments

This work was supported by NSF grant EAR-1260916 and the Carnegie Institution of Washington's Department of Terrestrial Magnetism. We thank Karl Karlstrom and Brandon Schmandt for their constructive reviews of an earlier version of this manuscript and two anonymous reviewers for their input. Additionally, we acknowledge the following groups for collecting and archiving the data for this project, IRIS (Data Management Center), the Caltech Regional Seismic Network, the EarthScope USArray Transportable Array, the University of Utah Network, the Sierra Nevada EarthScope Project (SNEP) Array [*Gilbert et al.*, 2007], the Colorado Plateau-Great Basin Network, the Coso Passive Short Period Arrays, the Rio Grande Seismic Transect Extension (RISTRA) Array [*Wilson et al.*, 2010], the Ruby Mountains Seismic Experiment [*Litherland et al.*, 2011], the Sierran Paradox Array [*Boyd et al.*, 2004], the Sandia Leo Brady Network, the Western Great Basin/Eastern Sierra Nevada Network, and the United States Advanced National Seismic System. Many of the figures were made using the Generic Mapping Tools (GMT) Program [*Wessel and Smith*, 1998].

References

Armstrong, R., and P. Ward (1991), Evolving geographic patterns of Cenozoic magmatism in the North American Cordillera: The temporal and spatial association of magmatism and metamorphic core complexes, *J. Geophys. Res.*, *96*(B8), 13,201–13,224.

Barmin, M. P., M. H. Ritzwoller, and A. L. Levshin (2001), A fast and reliable method for surface wave tomography, *Pure Appl. Geophys.*, *158*(8), 1351–1375.

Becker, T. W., C. Faccenna, E. D. Humphreys, A. R. Lowry, and M. S. Miller (2013), Static and dynamic support of western United States topography, *Earth Planet. Sci. Lett.*, In Press.

Bedrosian, P. A., and D. W. Feucht (2013), Structure and tectonics of the northwestern United States from EarthScope USArray magnetotelluric data, *Earth Planet. Sci. Lett.*, In Press.

Bennett, R. A., B. P. Wernicke, N. A. Niemi, A. M. Friedrich, and J. L. Davis (2003), Contemporary strain rates in the northern Basin and Range province from GPS data, *Tectonics*, *22*(2), 1008, doi: 10.1029/2001TC001355.

Bensen, G. D., M. H. Ritzwoller, M. P. Barmin, A. L. Levshin, F. Lin, M. P. Moschetti, N. M. Shapiro, and Y. Yang (2007), Processing seismic ambient noise data to obtain reliable broad band surface wave dispersion measurements, *Geophys. J. Int.*, *169*(3), 1239–1260.

Best, M. G., and E. H. Christiansen (1991), Limited extension during peak tertiary volcanism, Great-Basin of Nevada and Utah, *J. Geophys. Res.*, *96*(B8), 13,509–13,528.

Best, M. G., E. H. Christiansen, and S. Gromme (2013), Introduction: The 36–18 Ma southern Great Basin, USA, ignimbrite province and flareup: Swarms of subduction-related supervolcanoes, *Geosphere*, *9*(2), 260–274.

Bina, C. R., S. Stein, F. C. Marton, and E. M. Van Ark (2001), Implications of slab mineralogy for subduction dynamics, *Phys. Earth Planet. Inter.*, *127*(1), 51–66.

Blackwell, D. D., and M. Richards (2004), Geothermal Map of North America, 1 sheet, scale 1:6,500,000, *Am. Assoc. Petrol. Geol.*, Tulsa, Oklahoma.

Boyd, O. S., C. H. Jones, and A. F. Sheehan (2004), Foundering lithosphere imaged beneath the southern Sierra Nevada, California, USA, *Science*, *305*(5684), 660–662.

Buehler, J. S., and P. M. Shearer (2010), Pn tomography of the western United States using USArray, *J. Geophys. Res.*, *115*, B09315, doi: 10.1029/2009JB006874.

Christensen, N. I. (1996), Poisson's ratio and crustal seismology, *J. Geophys. Res.*, *101*(B2), 3139–3156.

Christiansen, R. L., and E. H. McKee (1978), Late Cenozoic volcanic and tectonic evolution of the Great Basin and Columbia Intermontane regions, *Mem. Geol. Soc. Am.*, *152*, 283–311.

Coney, P. J., and T. A. Harms (1984), Cordilleran metamorphic core complexes: Cenozoic extensional relics of Mesozoic compression, *Geology*, *12*(9), 550–554.

Coney, P. J., and S. J. Reynolds (1977), Cordilleran benioff zones, *Nature*, *270*, 403–406.

DeCelles, P. G. (2004), Late Jurassic to Eocene evolution of the Cordilleran thrust belt and foreland basin system, western USA, *Am. J. Sci.*, *304*(2), 105–168.

Deschamps, F., J. Trampert, and R. Snieder (2002), Anomalies of temperature and iron in the uppermost mantle inferred from gravity data and tomographic models, *Phys. Earth Planet. Inter.*, *129*(3–4), 245–264.
Dickinson, W. R. (2002), The Basin and Range province as a composite extensional domain, *Int. Geol. Rev.*, *44*(1), 1–38.
Dickinson, W. R. (2006), Geotectonic evolution of the Great Basin, *Geosphere*, *2*(7), 353–368.
Dickinson, W. R., and W. S. Snyder (1979), Geometry of subducted slabs related to San-Andreas transform, *J. Geol.*, *87*(6), 609–627.
Dilek, Y., and E. M. Moores (1999), A Tibetan model for the early Tertiary western United States, *J. Geol. Soc.*, *156*(5), 929–941.
Dueker, K. G., and A. F. Sheehan (1997), Mantle discontinuity structure from midpoint stacks of converted P to S waves across the Yellowstone hotspot track, *J. Geophys. Res.*, *102*(B4), 8313–8327.
Egger, A. E., T. A. Dumitru, E. L. Miller, C. F. I. Savage, and J. L. Wooden (2003), Timing and nature of tertiary plutonism and extension in the grouse creek mountains, Utah, *Int. Geol. Rev.*, *45*(6), 497–532.
Elkins-Tanton, L. T. (2005), Continental magmatism caused by lithospheric delamination, in *GSA Special Paper 388: Plates, Plumes and Paradigms*, edited by G. R. Foulger et al., pp. 449–461, Geol. Soc. Am., Boulder, Colo.
Forsyth, D., S. Webb, L. Dorman, and Y. Shen (1998), Phase velocities of Rayleigh waves in the MELT experiment on the East Pacific Rise, *Science*, *280*(5367), 1235–1238.
Foster, D. A., P. A. Mueller, D. W. Mogk, J. L. Wooden, and J. J. Vogl (2006), Proterozoic evolution of the western margin of the Wyoming craton: Implications for the tectonic and magmatic evolution of the northern Rocky Mountains, *Can. J. Earth Sci.*, *43*(10), 1601–1619.
Gilbert, H. (2012), Crustal structure and signatures of recent tectonism as influenced by ancient terranes in the western United States, *Geosphere*, *8*(1), 141–157.
Gilbert, H., C. Jones, T. J. Owens, and G. Zandt (2007), Imaging Sierra Nevada lithospheric sinking, *Eos Trans. AGU*, *88*(21), 225–229.
Gilbert, H. J., A. F. Sheehan, K. G. Dueker, and P. Molnar (2003), Receiver functions in the western United States, with implications for upper mantle structure and dynamics, *J. Geophys. Res.*, *108*(B5), 2229, doi: 10.1029/2001JB001194.
Griffin, W. L., S. Y. O'Reilly, B. J. Doyle, N. J. Pearson, H. Coopersmith, K. Kivi, V. Malkovets, and N. Pokhilenko (2004), Lithosphere mapping beneath the North American plate, *Lithos*, *77*(1–4), 873–922.
Griffin, W. L., S. Y. O'Reilly, J. C. Afonso, and G. C. Begg (2009), The composition and evolution of lithospheric mantle: A re-evaluation and its tectonic implications, *J. Petrol.*, *50*, 1185–1204.
Hales, T. C., D. L. Abt, E. D. Humphreys, and J. J. Roering (2005), A lithospheric instability origin for Columbia River flood basalts and Wallowa Mountains uplift in northeast Oregon, *Nature*, *438*, 842–845.
Herrmann, R. B. (1987), *Computer Programs in Seismology*, St. Louis Univ., St. Louis, Mo.
Humphreys, E., E. Hessler, K. Dueker, G. L. Farmer, E. Erslev, and T. Atwater (2003), How Laramide-age hydration of North American lithosphere by the Farallon slab controlled subsequent activity in the western United States, *Int. Geol. Rev.*, *45*(7), 575–595.
Humphreys, E. D. (1995), Post-Laramide removal of the Farallon slab, western United States, *Geology*, *23*(11), 987–990.
Humphreys, E. D., and K. G. Dueker (1994), Physical state of the western US upper mantle, *J. Geophys. Res.*, *99*(B5), 9635–9650.
James, D. E., M. J. Fouch, R. W. Carlson, and J. B. Roth (2011), Slab fragmentation, edge flow and the origin of the Yellowstone hotspot track, *Earth Planet. Sci. Lett.*, *311*(1–2), 124–135.
Kerr, A. C. (1994), Lithospheric thinning during the evolution of continental large igneous provinces: A case study from the North Atlantic Tertiary province, *Geology*, *22*(11), 1027–1030.
Kistler, R. W., and Z. E. Peterman (1978), Reconstruction of crustal blocks of California on the basis of initial strontium isotopic compositions of Mesozoic granitic rocks, *U.S. Geol. Surv. Prof. Pap, 1071*, 17 pp.
Levander, A., and M. S. Miller (2012), Evolutionary aspects of lithosphere discontinuity structure in the western U.S., *Geochem. Geophys. Geosyst.*, *13*, Q0AK07, doi:10.1029/2012GC004056.
Levander, A., B. Schmandt, M. S. Miller, K. Liu, K. E. Karlstrom, R. S. Crow, C. T. A. Lee, and E. D. Humphreys (2011), Continuing Colorado plateau uplift by delamination-style convective lithospheric downwelling, *Nature*, *472*(7344), 461–465.
Ligorria, J. P., and C. J. Ammon (1999), Iterative deconvolution and receiver-function estimation, *Bull. Seismol. Soc. Am. 89*, 1395–1400.
Lin, F.-C., M. H. Ritzwoller, Y. Yang, M. P. Moschetti, and M. J. Fouch (2010), Complex and variable crustal and uppermost mantle seismic anisotropy in the western United States, *Nat. Geosci.*, *4*(1), 55–61.
Litherland, M., S. Klemperer, and J. Lawrence (2011), Crustal structure of the Ruby Mountains core complex from seismic observations, Abstract S41A-2156 presented at 2011 Fall Meeting, AGU, San Francisco, Calif.
Lowry, A. R., and M. Pérez-Gussinyé (2011), The role of crustal quartz in controlling Cordilleran deformation, *Nature*, *471*(7338), 353–357.
McKee, E. H., D. C. Noble, and M. L. Silberman (1970), Middle Miocene hiatus in volcanic activity in the Great Basin area of the western United States, *Earth Planet. Sci. Lett.*, *8*(2), 93–96.
Moschetti, M. P., M. H. Ritzwoller, F. C. Lin, and Y. Yang (2010), Crustal shear wave velocity structure of the western United States inferred from ambient seismic noise and earthquake data, *J. Geophys. Res.*, *115*, B10306, doi:10.1029/2010JB007448.
Mueller, P. A., J. L. Wooden, D. W. Mogk, and D. A. Foster (2011), Paleoproterozoic evolution of the Farmington zone: Implications for terrane accretion in southwestern Laurentia, *Lithosphere*, *3*(6), 401–408.
Noble, D. C. (1972), Some observations on the Cenozoic volcano-tectonic evolution of the Great Basin, western United States, *Earth Planet. Sci. Lett.*, *17*(1), 142–150.
O'Driscoll, L. J., E. D. Humphreys, and B. Schmandt (2011), Time corrections to teleseismic P delays derived from SKS splitting parameters and implications for western US P-wave tomography, *Geophys. Res. Lett.*, *38*, L19304, doi:10.1029/2011GL049031.
O'Reilly, S. Y., and W. L. Griffin (2006), Imaging global chemical and thermal heterogeneity in the subcontinental lithospheric mantle with garnets and xenoliths: Geophysical implications, *Tectonophysics*, *416*(1–4), 289–309.
Obrebski, M., R. M. Allen, F. Pollitz, and S. H. Hung (2011), Lithosphere-asthenosphere interaction beneath the western United States from the joint inversion of body wave traveltimes and surface wave phase velocities, *Geophys. J. Int.*, *185*, 1003–1021, doi:10.1111/j.1365-246X.2011.04990.x.
Owens, T. J., H. P. Crotwell, C. Groves, and P. Oliver-Paul (2004), SOD: Standing order for data, *Seismol. Res. Lett.*, *75*(4), 515–520.
Pollack, H. N. (1986), Cratonization and thermal evolution of the mantle, *Earth Planet. Sci. Lett.*, *80*(1–2), 175–182.
Pollitz, F., and J. A. Snoke (2010), Rayleigh-wave phase-velocity maps and three-dimensional shear velocity structure of the western US from local non-plane surface wave tomography, *Geophys. J. Int.*, *180*(3), 1153–1169.
Porter, R., H. Gilbert, G. Zandt, S. Beck, L. Warren, J. Calkins, P. Alvarado, and M. Anderson (2012), Shear wave velocities in the Pampean flat-slab region from Rayleigh wave tomography: Implications for slab and upper mantle hydration, *J. Geophys. Res.*, *117*, B11301, doi: 10.1029/2012JB009350.
Roth, J. B., M. J. Fouch, D. E. James, and R. W. Carlson (2008), Three-dimensional seismic velocity structure of the northwestern United States, *Geophys. Res. Lett.*, *35*, L15304, doi:10.1029/2008GL034669.

Saltus, R. W., and G. A. Thompson (1995), Why is it downhill from Tonopah to Las Vegas?: A case for mantle plume support of the high northern Basin and Range, *Tectonics*, *14*(6), 1235–1244.
Savage, M. K., and A. F. Sheehan (2000), Seismic anisotropy and mantle flow from the Great Basin to the Great Plains, western United States, *J. Geophys. Res.*, *105*(B6), 13,715–13,734.
Schmandt, B., and E. Humphreys (2010), Complex subduction and small-scale convection revealed by body-wave tomography of the western United States upper mantle, *Earth Planet. Sci. Lett.*, *297*(3–4), 435–445.
Schruben, P. G., R. E. Arndt, W. J. Bawiec, P. B. King, and H. M. Beikman (1994), *Geology of the Conterminous United States at 1:2,500,000 Scale: A Digital Representation of the 1974 P.B. King and H.M. Beikman Map*, U.S. Geol. Surv., Reston, Va.
Shapiro, N. M., M. Campillo, L. Stehly, and M. H. Ritzwoller (2005), High-resolution surface-wave tomography from ambient seismic noise, *Science*, *307*(5715), 1615–1618.
Shen, W., M. H. Ritzwoller, and V. Schulte-Pelkum (2013), A 3-D model of the crust and uppermost mantle beneath the Central and Western US by joint inversion of receiver functions and surface wave dispersion, *J. Geophys. Res.*, *118*, 262–276, doi:10.1029/2012JB009602.
Sigloch, K. (2011), Mantle provinces under North America from multifrequency P wave tomography, *Geochem. Geophys. Geosyst.*, *12*, Q02W08, doi:10.1029/2010GC003421.
Snoke, J. A., and D. E. James (1997), Lithospheric structure of the Chaco and Paraná Basins of South America from surface-wave inversion, *J. Geophys. Res.*, *102*(B2), 2939–2951.
Sonder, L. J., and C. H. Jones (1999), Western United States extension: How the west was widened, *Annu. Rev. Earth Planet. Sci.*, *27*(1), 417–462.
Trabant, C., A. R. Hutko, M. Bahavar, R. Karstens, T. Ahern, and R. Aster (2012), Data products at the IRIS DMC: Stepping stones for research and other applications, *Seismol. Res. Lett.*, *83*(5), 846–854.
Wannamaker, P. E., D. P. Hasterok, J. M. Johnston, J. A. Stodt, D. B. Hall, T. L. Sodergren, L. Pellerin, V. Maris, W. M. Doerner, and K. A. Groenewold (2008), Lithospheric dismemberment and magmatic processes of the Great Basin-Colorado Plateau transition, Utah, implied from magnetotellurics, *Geochem. Geophys. Geosyst.*, *9*, Q05019, doi:10.1029/2007GC001886.
Warren, L. M., J. A. Snoke, and D. E. James (2008), S-wave velocity structure beneath the High Lava Plains, Oregon, from Rayleigh-wave dispersion inversion, *Earth Planet. Sci. Lett.*, *274*(1–2), 121–131.
Wernicke, B., J. L. Davis, N. A. Niemi, P. Luffi, and S. Bisnath (2008), Active megadetachment beneath the western United States, *J. Geophys. Res.*, *113*, B11409, doi:10.1029/2007JB005375.
Wessel, P., and W. H. F. Smith (1998), New, improved version of Generic Mapping Tools released, *Eos Trans. AGU*, *79*, 579.
West, J. D., M. J. Fouch, J. B. Roth, and L. T. Elkins-Tanton (2009), Vertical mantle flow associated with a lithospheric drip beneath the Great Basin, *Nat. Geosci.*, *2*(6), 438–443.
Whitmeyer, S. J., and K. E. Karlstrom (2007), Tectonic model for the Proterozoic growth of North America, *Geosphere*, *3*(4), 220–259.
Wilson, D. C., R. Aster, S. Grand, J. Ni, and W. S. Baldridge (2010), High-resolution receiver function imaging reveals Colorado Plateau lithospheric architecture and mantle-supported topography, *Geophys. Res. Lett.*, *37*(20), L20313, doi:10.1029/2010GL044799.
Wüstefeld, A., G. Bokelmann, G. Barruol, and J. P. Montagner (2009), Identifying global seismic anisotropy patterns by correlating shear-wave splitting and surface-wave data, *Phys. Earth Planet. Inter.*, *176*(3–4), 198–212.
Yuan, H., and B. Romanowicz (2010a), Depth dependent azimuthal anisotropy in the western US upper mantle, *Earth Planet. Sci. Lett.*, *300*(3), 385–394.
Yuan, H., and B. Romanowicz (2010b), Lithospheric layering in the North American craton, *Nature*, *466*(7310), 1063–1068.
Yuan, H., B. Romanowicz, K. M. Fischer, and D. Abt (2011), 3-D shear wave radially and azimuthally anisotropic velocity model of the North American upper mantle, *Geophys. J. Int.*, *184*(3), 1237–1260.
Zandt, G. (2003), The southern Sierra Nevada drip and the mantle wind direction beneath the southwestern United States, *Int. Geol. Rev.*, *45*(3), 213–224.
Zandt, G., and E. Humphreys (2008), Toroidal mantle flow through the western US slab window, *Geology*, *36*(4), 295–298.
Zandt, G., S. C. Myers, and T. C. Wallace (1995), Crust and mantle structure across the Basin and Range-Colorado Plateau boundary at 37 N latitude and implications for Cenozoic extensional mechanism, *J. Geophys. Res.*, *100*(B6), 10,529–10,548.
Zhao, G., M. Sun, S. A. Wilde, and S. Li (2004), A Paleo-Mesoproterozoic supercontinent: Assembly, growth and breakup, *Earth Sci. Rev.*, *67*(1–2), 91–123.
Zhu, L., and H. Kanamori (2000), Moho depth variation in southern California from teleseismic receiver functions, *J. Geophys. Res.*, *105*(B2), 2969–2980.
Zoback, M. L., R. E. Anderson, and G. A. Thompson (1981), Cainozoic evolution of the state of stress and style of tectonism of the Basin and Range province of the western United States, *Philos. Trans. R. Soc. London A*, *300*(1454), 407–434.